Applied Surface Science 600 (2022) 154081

Contents lists available at ScienceDirect

Applied Surface Science

journal homepage: www.elsevier.com/locate/apsusc

Full Length Article

Bridging experiment and theory: Morphology, optical, electronic, and magnetic properties of $MnWO_4$

Marcelo Assis [a,*], Ana C.M. Tello [b,c], Fabio S.A. Abud [d], Pablo Negre [b], Lara K. Ribeiro [a,b], Renan A.P. Ribeiro [e], Sueli H. Masunaga [d,f], Aline E.B. Lima [g], Geraldo E. Luz Jr [g], Renato F. Jardim [d], Albérico B.F. Silva [c], Juan Andrés [a], Elson Longo [b]

[a] Departament of Physical and Analytical Chemistry, University Jaume I (UJI), Castelló 12071, Spain
[b] CDMF, LIEC, Chemistry Department of the Federal University of São Carlos (UFSCar), 13565-905 São Carlos, SP, Brazil
[c] Institute of Chemistry of São Carlos, University of São Paulo (USP), 13566-590 São Carlos, SP, Brazil
[d] Institute of Physics, University of São Paulo (USP), Rua do Matão 1371, 05508-090 São Paulo, SP, Brazil
[e] Department of Chemistry, Minas Gerais State University (UEMG), 35501-170 Divinópolis, MG, Brazil
[f] Department of Physics, Centro Universitário FEI, 05508-090 S. B. do Campo, SP, Brazil
[g] Departament of Chemistry (DQ), Federal University of Piauí (UFPI), Teresina, Piauí 64049-550, Brazil

ARTICLE INFO

Keywords:
$MnWO_4$
Density functional theory
Surface structure
Morphology
Optical
Electronic and magnetic properties

ABSTRACT

Manganese tungstate ($MnWO_4$) compounds have gathered tremendous interest in the research community due to their wide range of applications. Herein, we show a comprehensive experimental, theoretical and computational study aimed at providing an in-depth understanding of the morphology as well as optical, electronic and magnetic properties of monoclinic $MnWO_4$. In order to evaluate such properties together with the geometry and vibrational frequencies of these materials, first-principles calculations were used at the DFT level. The synthesis and analysis of these properties were then featured by (i) the composition, geometry, and electronic and magnetic structure of the exposed surfaces at the morphology based on the different numbers of unsaturated superficial Mn and W cations (local coordination, i.e., clusters) of each surface, and (ii) the determination of the energy profiles associated with the transformation process between different morphologies. Additionally, we used a combination of theories and simulations to link experimental results to a prediction of the corresponding properties. These system-specific findings at the atomic level provide a powerful insight for understanding and tuning optical/electronic/magnetic properties of $MnWO_4$-based materials.

1. Introduction

Multiferroic materials, which can be characterized by the coexistence of ferroelectricity or ferroelasticity and magnetic order, have attracted great attention, both experimentally and theoretically. A good example of this family is the manganese wolframate, $MnWO_4$, which from the scientific point of view is of paramount importance because of its wide application as electrocatalysts, photocatalysts and battery material [1–7].

$MnWO_4$ is a type-II multiferroic material, meaning that the ferroelectricity occurs in conjunction with a cycloidal spiral magnetic phase. There, spin-frustrated antiferromagnetic phases (AF1, AF2 and AF3) are observed for $MnWO_4$ at low temperatures. Additionally, it has been established that the competing long-range interactions within the zigzag spin chains along the *c* axis and between spin chains along the *a* axis control the magnetic properties of the material [8]. In the AF1 phase, which occurs below T = 8.0 K, a collinear spin arrangement along chains is observed. On the other hand, the AF2 phase, which occurs between T = 8.0 K and T = 12.3 K, is characterized by an elliptical spiral spin structure along the chain with a spontaneous electric polarization. The AF3 phase, observed in a narrow temperature interval between 12.3 and 13.5 K, is characterized by a portion of the spins collinearly ordered along the *c* axis [8].

$MnWO_4$ has been synthetized by different techniques, including surfactant-free complexation-precipitation hydrothermal method [9], hydrothermal method [2–4,10], sonochemical synthesis, polyol-mediated low-temperature synthesis [11], microwave-assisted spray synthesis [12], surfactant-free precipitation method [1], microwave-

* Corresponding author.
E-mail address: marcelostassis@gmail.com (M. Assis).

https://doi.org/10.1016/j.apsusc.2022.154081
Received 23 March 2022; Received in revised form 8 June 2022; Accepted 25 June 2022
Available online 4 July 2022

assisted hydrothermal synthesis [11], solid-state metathetic approach [13], sol–gel [14], simple precipitation reaction [15], spark plasma sintering [5], and solvothermal method [16]. Particular interest has been paid to the improvement of optical and magnetic properties through synthesis conditions to obtain crystals with desired size and morphology, such as nanorods [17], nanowires [18], microspheres and nanoparticles [5,6].

Our group are engaged in a research field, combining theory, simulation and experiments, devoted to find a relationship among the magnetic properties of a given material and its magnetic moment [19–26]. Here, theoretical calculations based on the density functional theory (DFT) have been carried out to investigate the electronic structure and optical properties of bulk $MnWO_4$ and the pressure effects on these properties [27,28], in addition to polaron formation. Furthermore, the (0 1 0), (0 0 1), and (1 0 0) surfaces have been studied at the theoretical level to obtain information on their structure, energies and electronic properties, as well as their influence on the absorption of anionic collectors [29,30].

To the best of our knowledge, the literature lacks studies on the relationship among morphology, electronic and magnetic properties of $MnWO_4$. A deep understanding of these characteristics at the atomic level is an essential prerequisite for tuning their functions, and consequently their practical applications. Herein, we elucidate these points by performing a detailed theoretical and experimental study. The $MnWO_4$ samples were synthesized by the coprecipitation method (CP), followed by microwave irradiation (MI). The as-synthesized samples were characterized by X-ray diffraction (XRD) with Rietveld refinement, field emission scanning electron microscopy (FE-SEM), micro-Raman, and X-Ray photoelectron spectroscopy (XPS). Moreover, their optical properties were investigated by ultraviolet–visible (UV–vis) spectroscopy and PL measurements. First-principles calculations within the framework of density functional theory (DFT) were employed to obtain atomic-level information on geometry, electronic structure, local bonding, band structure, density of states (DOS), and vibrational frequencies of the materials. The morphologies of the samples were obtained by FE-SEM, and their corresponding transformations were rationalized by using the Wulff construction and altering the relative surface energy values of the (0 0 1), (0 1 0), (1 0 0), (0 1 1), (1 0 1), (1 1 0), (0 1 2) and (1 1 1) surfaces. Furthermore, the crystal structures, morphology, and optical, electronic and magnetic properties of $MnWO_4$ were analyzed by combining the results obtained from first-principles calculations and experimental measurements. This paper is comprised of three more sections. The experimental section elucidates the synthesis, characterization, computational details and model systems. The third section presents and discusses the results. Lastly, the fourth section summarizes the main conclusions.

2. Experimental section

Synthesis: 1×10^{-3} mol of $Na_2WO_4{\cdot}2H_2O$ (Sigma-Aldrich, 99.9%) was diluted in 50 mL of distilled water. Meanwhile, 1×10^{-3} mol of $MnCl_2{\cdot}4H_2O$ (Sigma-Aldrich, 99%) was added in another beaker. Then, the $MnCl_2{\cdot}4H_2O$ solution was added to the $Na_2WO_4{\cdot}2H_2O$ solution under stirring, and a brown precipitate was formed. The obtained system was transferred to a Teflon autoclave, sealed, and placed in the microwave-assisted hydrothermal system (2.45 GHz, maximum power of 800 W). The reaction mixtures were heated to 160 °C for five different MI time intervals: 2, 4, 8, 16 and 32 min. The final precipitate was washed several times with distilled water and dried at 60 °C for 24 h.

Characterizations: The samples were characterized by X-ray diffraction (XRD) using a D/Max-2500PC diffractometer (Rigaku, Japan) with Cu Kα radiation (λ = 1.54056 Å) in the 2θ range of 10–80° at a scan rate of 0.01° min^{-1}. Micro-Raman spectroscopy was carried out on an iHR550 spectrometer (Horiba Jobin-Yvon, Japan) with a charge-coupled device detector and an argon-ion laser (MellesGriot, USA) operating at 514.3 nm with a power of 200 mW. The field emission scanning electron microscopy (FE-SEM) images were analyzed using a FEI instrument (Model Inspect F50) operating at 5 kV. High-resolution transmission electron microscopy (HR-TEM) images were acquired on a JEM-2100F LaB6 (Joel) microscope operating at 200 kV. Ultraviolet–visible diffusion reflectance spectroscopy (UV–vis DRS) spectra were recorded using a Varian spectrophotometer (Varian, model Cary 5 G). PL measurements at room temperature were performed using a Monospec 27 monochromator (Thermal Jarrel Ash, USA) coupled to an R446 photomultiplier (Hamamatsu, Japan). XPS measurements were made on a Scientia Omicron ESCA spectrometer (Germany) using a monochromatic Al Kα X-ray source (1486.7 eV). All peaks were calibrated with reference to the C 1 s at 284.3 eV.

Magnetic measurements: Magnetization measurements as a function of temperature, M(T), and applied magnetic field, M(H), were performed in powder samples using the vibrating sample magnetometer option of the Dyna Cool-Physical Property Measurement System (*PPMS*) from Quantum Design equipped with a 90 kOe magnet. M(T) curves were taken under zero-field-cooling (ZFC) and field-cooling (*FC*) conditions with magnetic fields ranging from ~ 1000 Oe to 90 kOe and in the temperature range from 2 to 300 K. For the ZFC measurements, the samples were first cooled to 2 K in zero magnetic field. Then, a magnetic field was applied, and the M vs T data were recorded upon warming to ~300 K. The FC data were collected upon cooling to 2 K following the ZFC cycle. After cooling the powder samples in zero applied magnetic field, M(H) curves were taken at selected temperatures ranging from 2 to 300 K and magnetic fields between −90 and +90 kOe.

Computational details: In this work, the crystal structure of $MnWO_4$ was studied by first-principle calculations at the DFT level using hybrid exchange–correlation functional developed by Lee, Yang and Parr (B3LYP) [31], as implemented in the periodic *ab-initio* code CRYSTAL14 [32]. We performed previously an analysis of the band gap values obtained by different functionals (such as B3LYP, PBE0 and PBEsol0), we found that B3LYP functional render the closest value to experimental one, as it was reported in studies on complex metal oxides [19,33–37]. Extended Gaussian basis sets type 86-411d41G and 8-411 [38] were used for the manganese and oxygen atoms, respectively, while the large-effective core pseudopotential derived by Hay and Wadt [39] was chosen for tungsten. The calculations were performed with tolerances set to 10^{-8}, 10^{-8}, 10^{-8}, 10^{-8} and 10^{-16} in order to ensure high numerical accuracy in the Coulomb and exchange integral calculations. To provide an accurate description of the electronic structure, the Mohnkhost-Pack [40] network was defined as 8, featuring eight k-points to describe the high-symmetry reciprocal space. $MnWO_4$ belongs to the monoclinic space group P2/c with a wolframite structure. The optimized geometry was obtained by considering a total relaxation of the lattice parameters and atomic positions. The unit cell of $MnWO_4$ is comprised of two Mn atoms with a $3d^5$ electronic configuration. The high spin state (sextet) was considered for each Mn atom in all calculations.

To determine the magnetic order of the fundamental state of the material, two collinear magnetic configurations were studied: (i) ferromagnetic (*FM*), where the spins of all neighbors are ordered in parallel; and (ii) antiferromagnetic (*AFM*), where the nearest-neighbor spins ordered in an antiparallel manner in relation to each other.

The exchange coupling constant (J_{ij}) is based on the energy difference between the two models by using the Ising model: [19]

$$\boldsymbol{H}_{ising} = \sum \boldsymbol{J}_{ij}\boldsymbol{S}_{iz}\boldsymbol{S}_{jz} \quad (1)$$

The structural optimization was carried out considering the *FM* configuration, while the AFM configuration was computed as a single-point calculation based on the previously optimized geometry for FM to obtain the J_{ij} as a function of the energy difference between both models.

The vibrational modes and their corresponding frequencies were calculated by employing numerical second derivatives of total energies.

The structure of eight different surfaces of $MnWO_4$, i.e., the (0 0 1),

(0 1 0), (1 0 0), (0 1 1), (1 0 1), (1 1 0), (0 1 2) and (1 1 1) surfaces, and their influence on the morphology and properties were also investigated. Their surface energies (E_{surf}) were calculated by using a slab model. Convergence test for thickness of symmetrical and non-symmetrical slabs in FM state were simulated for all surfaces, and after the optimization process the slab with the lowest E_{surf} for each surface was chosen. As result, the number of layers considered for magnetic and surface energy analysis were: 50 (0 0 1), 28 (0 1 0), 30 (1 0 0), 60 (0 1 1), 55 (1 0 1), 60 (1 1 0), 60 (0 1 2) and 60 (1 1 1).

By using the optimized geometry of these slabs as predicted, we calculated the AFM state at the slab and determinated the magnetic order of the surface as in the bulk. The spin multiplicity ($2S + 1$) for each slab was also determined. The parameters of the chosen slabs can be found in **Table S1** in the Supporting Information.

The E_{surf} for the symmetrical slabs was calculated by using Eq. (2) as follows:

$$E_{surf} = \frac{E_{slab} - nE_{bulk}}{2A} \tag{2}$$

where E_{slab} is the total energy of the relaxed slab, E_{bulk} is the total energy of the bulk, n is the number of bulks in a slab, A is the surface area and number 2 refer to the two surfaces of the slab.

In the case of non-symmetrical slabs, the surface stability E_{surf} was considered equivalent to the energy associated with the cleavage of the crystal when the surface was created (E_{cleav}):

$$E_{cleav}^{unrlx} = \frac{E_{slab}^{unrlx} - nE_{bulk}}{2A} \tag{3}$$

where E_{slab}^{unrlx} and E_{bulk} are the total energy for the unrelaxed slab and the bulk unit, respectively. n and A have the same definition as those described in Eq. (2).

In case of thickness converged slabs, the outer layers exhibits the highest relaxation degree suggesting that the relaxation energy (E_{relax}) can be computed for the terminations Z^+ and Z^- was calculated as the difference between the energy of the relaxed and unrelaxed slabs:

$$E_{relax}(Z^+|Z^-) = \frac{E_{slab}^{unrlx} - E_{slab}^{relax}}{2A} \tag{4}$$

Thus, the E_{surf} is written by the mean value for both terminations:

$$E_{surf} = E_{cleav}^{relax}(Z^+|Z^-) = E_{cleav}^{unrlx} - E_{relax}(Z^+|Z^-) \tag{5}$$

In terms of the above approximation, the E_{surf} of several surfaces was calculated and the morphology was generated from the Wulff construction, considering a huge vacuum of 500 Å. The atom and electron properties of the material as well as the surfaces were analyzed through band structure and spin-polarized atom-resolved DOS. The structures were constructed along the high-symmetry directions of the corresponding irreducible Brillouin zone. Moreover, the density of the states and the band structure of the middle slab layers are similar to the bulk for all investigated surfaces. Although this model is rather simplistic (we do not consider the environment, i.e. the evaluation of the oxygen dependence evaluation via the chemical potential), it is very helpful in elucidating the available morphologies, as studied by first-principles DFT calculations.

The magnetic properties were analyzed by the magnetization density index (D_μ), defined as the number of unpaired electrons (μ_B) per unit area:

$$D_\mu = \frac{\mu_B}{A} \tag{6}$$

The total magnetization density index (M) was then calculated as follows:

$$M = \sum_i C_i^{(hkl)} \bullet D_\mu^{(hkl)}, \tag{7}$$

where $C_i^{(hkl)} = A^i/A$ is the percentage of contribution of each surface in the total surface area of the morphology studied.

This procedure has been performed to obtain the complete set of morphologies of different materials based on the Wulff construction and the values of E_{surf} and to investigate the magnetic and multiferroic properties of different materials [19,37,41–48], in addition to pathways connecting the different morphologies. The energy (E_{pol}) and band gap energy (E_{gap}^{poly}) of the polyhedron were calculated by assuming the contributions from each surface to the morphology ($C_i^{(hkl)}$) and the corresponding E_{surf}^{hkl} values and surface band gap energy (E_{gap}^{hkl}), respectively, as follows:

$$E_{pol} = \sum_i C_i \bullet E_{surf}^{hkl} \tag{8}$$

$$E_{gap}^{poly} = \sum_i C_i \bullet E_{gap}^{hkl} \tag{9}$$

3. Results and discussion

Through the analysis of XRD, XPS and Raman spectroscopy images, it was possible to observe that all samples belong to a wolframite-type monoclinic structure with space group P2/c.[3,49–51] According to the results obtained in the Rietveld refinement, a reduction in the crystalline cell occurs with increasing microwave irradiation (MI) time. These changes are responsible for symmetry breaking processes and increased short- and long-range disorder in $MnWO_4$ samples [52]. These results can be seen in detail in the Supporting Information (**Figs. S1-S3** and **Tables S2, S3 and S4**).

The structural order at medium range was investigated by photoluminescence (PL) measurements for all samples, and the spectra of $MnWO_4$ samples are displayed in Fig. 1.

As in several transition metal-tungstates from the wolframite group, the emission of $MnWO_4$ occurs through metal-to-metal charge transfer [53]. In $MnWO_4$, Mn^{2+} cations have 5 electrons in the 3*d* orbital with high spin configurations ($t_{2g}^3e_g^2$), whereas the 5*d* orbitals in W^{6+} are empty [54]. The picture that emerges from the analysis is that one electron from partially filled 3*d* orbital of the Mn is transferred to the unoccupied anti-bonding W *5d* states. For this reason, the unoccupied electronic states of $MnWO_4$ near the Fermi level would be composed of W 5*d* states and Mn 3*d* states. As it can be seen, all PL spectra exhibit broad bands covering the visible spectrum, which in turn emit a wide range of energies, further indicating typical multiphonon processes in semiconductors [55]. Therefore, excited and pre-excited electrons recombine with holes (electron/hole pair) by several paths due to the relaxation of electron/hole momentum by phonon emission, thus emitting photons with the corresponding energies [52,56]. According to **Fig. 1A, a** comparison between the PL intensities indicates that the emission intensities increase as a function of MI. Since the PL emission is assigned to structural disorder, the increase in PL intensities can be attributed to an increase in the degree of structural disorder [3,57], as observed in both XRD and Raman analyses, leading to a density of intermediate energy states within the band gap region. However, in case of a high density of these energy states, the contribution of non-radiative recombination processes increases, thus reducing the radiative recombination rate and the photon emission.

A more intense right shift of the band is also observed with increasing MI approximately from 462 to 494 nm, in addition to the appearance of a new band at 646 nm in sample $MnWO_4$-32. The displacement and formation of emission bands at longer wavelengths are due to the improved contributions of deep defects in the material, according to the broadband theory [48,58,59]. This emission is a result of the increase in the number of intermediate states close to the valence (VB) and conduction bands (CB), and may be related to the formation of oxygen vacancies (V_O) generated from the increase in the MI time of the $MnWO_4$

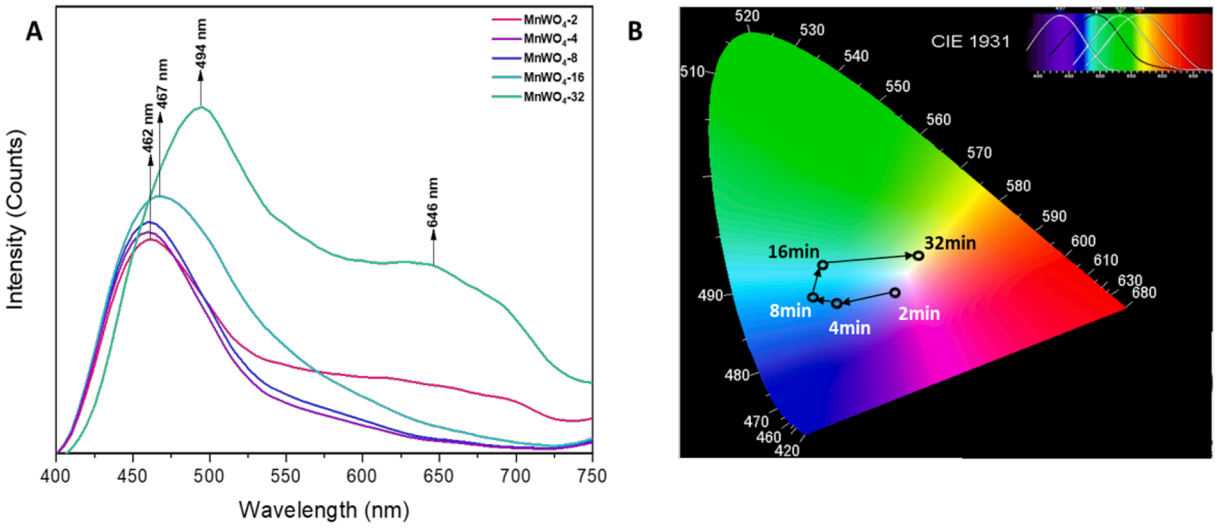

Fig. 1. **(A)** PL spectra obtained at room temperature with excitation of λ = 325 nm and **(B)** CIE chromaticity coordinates for the samples obtained through SpectraLux software.

samples. Such defects increase the short-, medium- and long-range disorder within the material, corroborating the structural results previously mentioned. The increase in deep defects can also be accompanied by a change in the emission of the materials, as shown in Fig. 1**B**, which displays the draft of terms and definitions for lighting issued by the *Commission Internationale de l'Éclairage* (CIE – International Commission on Illumination) [60]. At first, a blue shift occurs, followed by a yellow shift attributed to a greater contribution of the emission in the red region (deep defects). The values of x and y obtained for the samples synthesized at 2, 4, 8, 16 and 32 min were found to be (0.3219; 0.3098), (0.1924; 0.2748), (0.1980; 0.2646), (0.2178; 0.3294) and (0.3751; 0.3834), respectively.

The parameters employed during the synthesis of $MnWO_4$, such as temperature, solvent, pH, pressure, agitation and use of surfactants among others, were responsible for changes in the morphology and size of the obtained materials [61,62]. We observed through the PL measurements that the MI time in the $MnWO_4$ samples changes the nature of the defects, as it can analyzed with the morphology of $MnWO_4$ obtained by the images of FE-SEM (see Fig. 2**A-J)**. The $MnWO_4$ samples are comprised of 1D aggregates, being nanorods the main morphology observed. There is also a dependence between average particle size and MI time despite the high dispersion of sizes obtained. As the longer the MI time, the greater the particle size, yielding average length and width values of 48.1 ± 12.8 nm and 26.0 ± 5.2 nm, 49.9 ± 14.0 nm, and 27.8

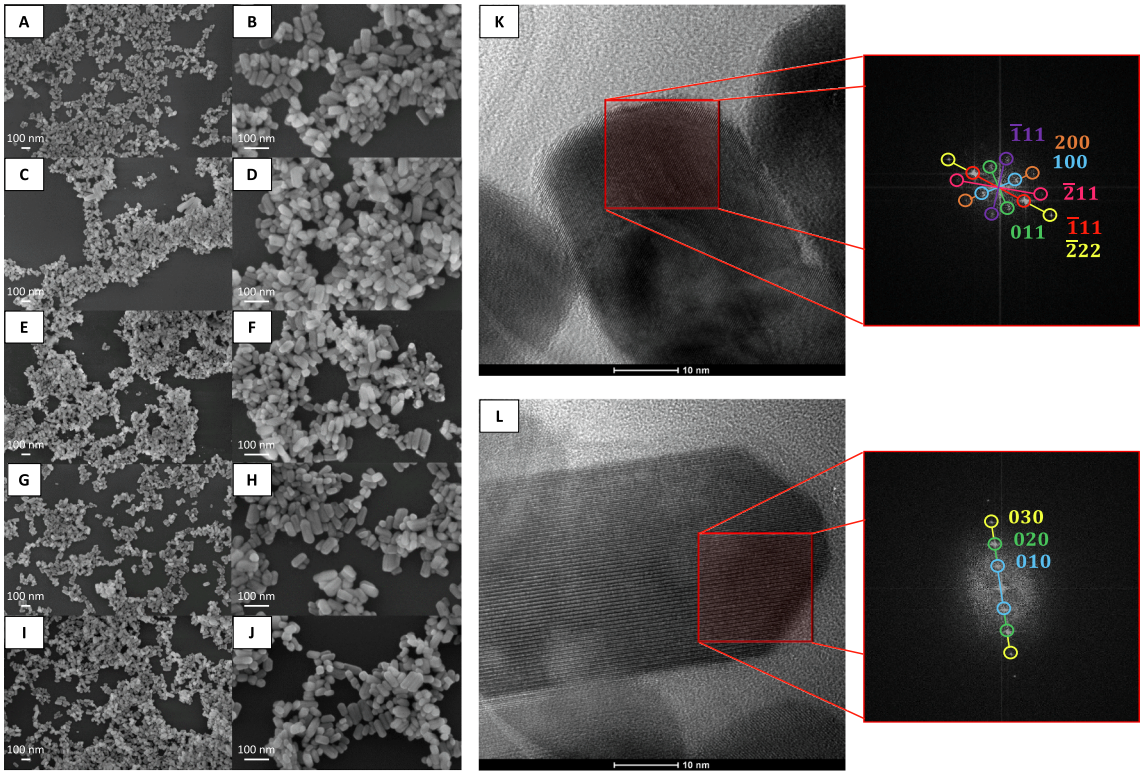

Fig. 2. FE-SEM of $MnWO_4$ samples synthesized by MI at (A-B) 2, (C-D) 4, (E-F) 8, (G-H) 16 and (I-J) 32 min. HR-TEM images of $MnWO_4$ synthesized at (K) 2 and (L) 32 min.

± 5.7 nm, 53.5 ± 12.4 nm and 28.0 ± 6.0 nm, 55.8 ± 12.3 nm and 28.4 ± 5.1 nm, 56.9 ± 11.2 nm and 29.8 ± 5.4 nm for samples synthesized at 2, 4, 8, 16 and 32 min, respectively. In order to clarify the resolution of the morphologies obtained as a result of the nanometric size and also to gain further information on the crystallinity of the samples, individual HR-TEM analyses were performed in samples synthesized at 2 (Fig. 2**K**) and 32 min (Fig. 2**L**). For the sample synthesized at 2 min, the $(\bar{1}11)$, (200), (100), $(\bar{2}11)$ and $(\bar{2}22)$ planes of the monoclinic phase of $MnWO_4$, referring to the distances of 2.99 Å, 2.41 Å, 4.82 Å, 2.04 Å and 1.49 Å, respectively, can be observed from the Fast Fourier Transform (FFT) analysis. Regarding the sample synthesized at 32 min, the preferential orientation of growth is found to be in the vicinity of the (0*k*0) planes, that is, the (010), (020), and (030) planes with interplanar distances of 5.75 Å, 2.87 Å, and 1.91 Å, respectively. In this way, the increase in MI causes the preferential growth of $MnWO_4$ crystals along the [0*k*0] directions due to the successive re-dilution and recrystallization processes that occur during the synthesis of $MnWO_4$ samples obtained at prolonged MI times. In this way, the morphology change can be associated to the appearance deep defects provoked by MI, which leads to the preferential growth of $MnWO_4$ samples in the (0k0) plane.

The magnetic properties of $MnWO_4$ nanorods were studied by analyzing the magnetization curves as a function of temperature (M/H) and applied magnetic fields [M(H)]. This analysis allows us to find a relationship among the magnetic properties, the morphology, and the change of defects from MI. A bulk-$MnWO_4$ compound exhibits a transition to antiferromagnetic (AF) order at $T_N = 13.5$ K, and undergoes at least two successive AF phase transitions at ~12.5 K and ~8.0 K [8]. Nevertheless, the $MnWO_4$ nanorods present solely one transition at T_N = 8.1, 8.5, 8.5, 9.0 and 9.1 K for samples synthesized at 2, 4, 8, 16 and 32 min, respectively, according to Fig. 3**A**. The suppression of the low AF phases may be due to the finite size effects of nanorods. T_N is defined here as the temperature at which a step-like change in the first derivative, dM/dT, is observed. In addition, the AF transition is broadened with increasing H. For H = 90 kOe, the transition to the AF phase is no longer noticed in the M/H curves for all samples, as shown in Fig. 3**B**. Other size effects are observed in these magnetization data, for instance, the irreversibility between the ZFC and FC curves and the occurrence of hysteresis in M(H) curves with a small coercive field (H_C) and a remanent magnetization (M_R). Fig. 3**A–B** show the ZFC and FC curves only for the sample synthesized at 2 min for the sake of clarity; however, it can be seen that the irreversibility between these curves occurs for all samples. Fig. 3**C** displays the hysteresis curves at 2 K for the $MnWO_4$ nanorods, where the following values can be observed: H_C = 60, 37, 50, 21 and 35 Oe, and M_R = (6.8, 3.9, 4.7, 3.6, and 3.8) × 10^{-4} μ_B for the samples synthesized at 2, 4, 8, 16 and 32 min, respectively. The M(H) curves measured at T ≥ 8 K are reversible, as expected for antiferromagnetic or paramagnetic systems.

The effective magnetic moment (μ_{eff}) and the Curie-Weiss temperature (Θ_{CW}) were obtained by applying the Curie-Weiss law to the temperature-dependent magnetization data as follows: $\chi = C/(T - \Theta_{CW})$, where C is the Curie constant related to μ_{eff}. The fitted μ_{eff} and Θ_{CW}, performed in the temperature interval comprehended between 100 and

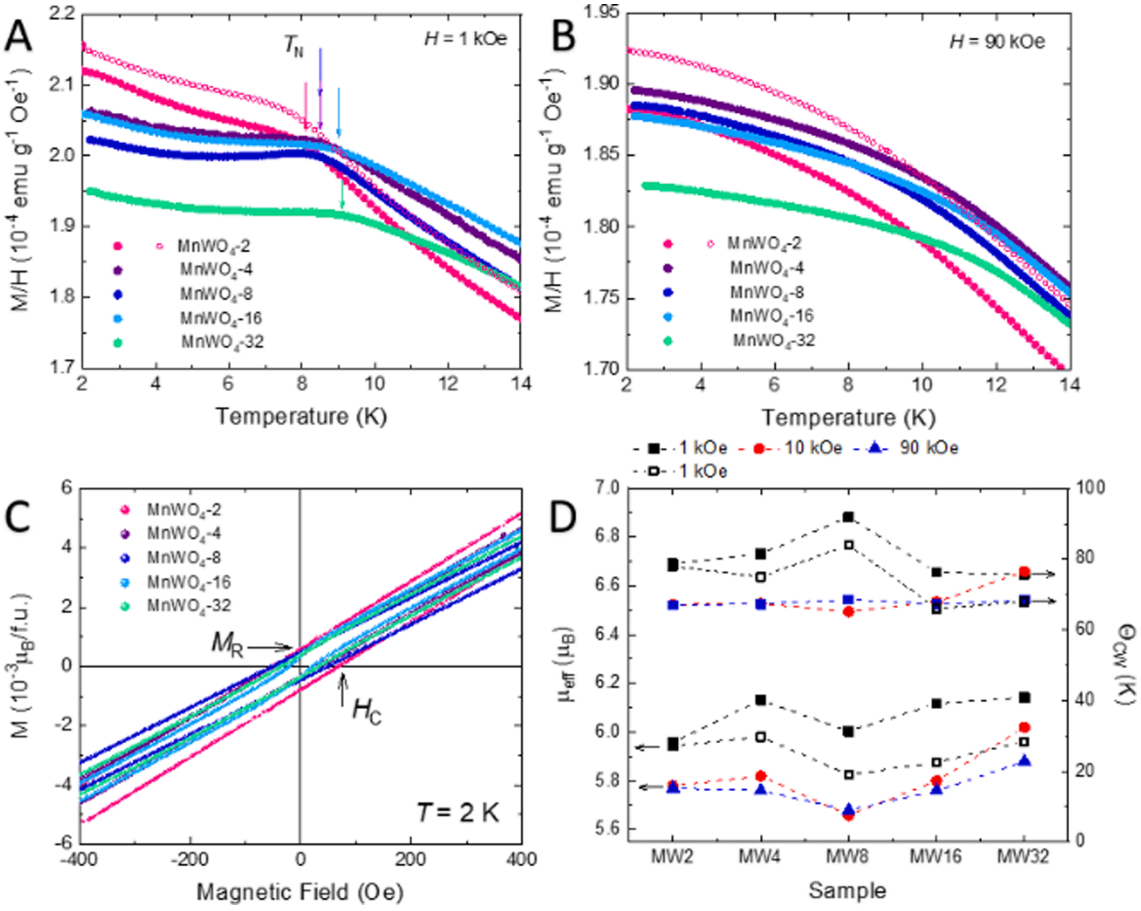

Fig. 3. ZFC magnetization curves measured in applied field of 1 kOe (A) and 90 kOe (B) for $MnWO_4$ samples. Only the FC curve for the sample synthesized at 2 min is plotted for the sake of clarity. (C) Expanded view of hysteresis M(H) cycles for the $MnWO_4$ sample at 2 K. (D) Closed symbols represent fitted μ_{eff} and Θ_{CW} values for different applied magnetic fields by using the Curie-Weiss law. Open symbols are μ_{eff} and Θ_{CW} obtained from the fitting of a modified Curie-Weiss law to the M/H curves under H = 1 kOe. The dashed lines are a guide to the eye.

300 K, resulted in different values for low and high fields, as displayed in Fig. 3**D**. For instance, similar values of μ_{eff} and Θ_{CW} were obtained from the data taken under 10 and 90 kOe for all samples. However, these values are relatively small in comparison with those acquired from the 1 kOe data. In the nanosized AF, surface spins may have multiple field-dependent configurations due to the exchange coupling between the surface and the core spins [63]. In addition, for the nanosized systems with size distribution the magnetization can be dominated by the contributions of larger particles in low fields and by magnetic interactions between the nanoparticles [64]. In this case, a modified Curie-Weiss law can be used to analyze the magnetic susceptibility measured in low fields according to the following equation: $\chi = \chi_0 + C/(T - \Theta_{CW})$, where χ_0 is a temperature-independent contribution [65]. By performing a fitting of this modified law to the 1 kOe data, μ_{eff} and Θ_{CW} approach the values obtained from the 10 and 90 kOe data, as displayed in open square symbols in Fig. 3**D**. Despite the initial higher values of μ_{eff} obtained from the 1 kOe data, the values between 5.96 and 6.14 μ_B are consistent with that of 5.90 μ_B expected for Mn^{2+} ($S = 5/2$) and the experimental ones between 5.68 and 6.20 μ_B reported for $MnWO_4$ samples [6,65].

The equilibrium lattice parameters (a, b, c, and β) were calculated by minimizing the crystal total energy (Table 1). Our calculated lattice parameters are in good agreement with those obtained from the experiments. The schematic representation of the $MnWO_4$ structure modeled through a 2x1x2 supercell with four-unit cells is illustrated in Fig. 4**.** The supercell model indicates that there are two separate blocks of distorted [MnO_6] and [WO_6] octahedral clusters connected by an oxygen ligand along its characteristic zigzag chain of edge-sharing [MnO_6] octahedra in the c axis. (Fig. 4**B**). The [MnO_6] octahedron has three different Mn–O bonding with bond lengths of 2.04 Å(2), 2.15 Å(2) and 2.35 Å(2). Similarly, the WO_6 octahedron has three different W–O bonding with bond lengths of 1.83 Å(2), 1.73 Å(2) and 2.37 Å(2). The experimental and theoretical results of lengths and bond angles are summarized in **Table S3**.

Based on the Heisenberg model [66], if the coupling constant is J > 0 (<0) the ground state is FM (AFM). The calculated local magnetic moment of the Mn atom is found to be 4.70 (4.71) μ_B, indicating that this atom possesses about + 5e charge with spin $S = 5/2$, which is consistent with the high spin $3d^5$ electron configuration of Mn. To establish the magnetic order of the ground state of $MnWO_4$, the total energy of both collinear AFM and FM models with spin multiplicities of 1 and 11, respectively, was calculated, and the results showed that the total energy of the AFM model is 16.71 eV lower than that of the FM model. The coupling constant value was found to be $J = -8.75K$, indicating that the ground state of $MnWO_4$ is AFM, meaning that an antiparallel coupling exists between two neighboring Mn atoms, which is congruent with the experimental findings [8,67,68]. To confirm the magnetic order of the material, a supercell 2x1x2 model was considered. This model consists of 8 Mn atoms with a $3d^5$ configuration as in the bulk (Fig. 4). The AFM configuration was modeled with the spins of Mn atoms ordered in parallel within the zigzag chains and in an antiparallel manner between adjacent chains. The FM state was also calculated with all spins of Mn atoms ordered in parallel, $2S + 1 = 41$. In this case, the coupling constant was found to be $J = -2.18K$, supporting the occurrence of an AFM ordering for the magnetic ground state of $MnWO_4$.

The electronic band structure along high-symmetry lines in the first Brillouin zone (BZ) and the total (partial) density of states (DOS) of the optimized structure of $MnWO_4$ are shown in Fig. 5. The electronic levels describing the electronic band structure exhibit an indirect band gap between the E (at the top of the valence band, VB) and the Γ points (at the bottom of the conduction band, CB) in the Brillouin zone. The value of the calculated band gap, 3.21 eV, is slightly higher than the experimental one, ~2.60 eV (Fig. 5**A**). This reduction in the experimentally observed optical band gap value may be related to distortions in the [WO_6] and [MnO_6] clusters, which favor the formation of intermediary energy states (photogenerated electron–hole pairs) between the VB and the CB. Moreover, the band structure is basically determined by the Mn 3d and 2p orbitals in the VB and the CB, mostly derived from Mn 5d, W 5d and O 2p orbitals.

By analyzing the band structure shown in Fig. 5**B** and the partial density of states in Fig. 5**C**, we can observe that the top of the VB is composed of the hybridization of $3d_{xz}$ and $3d_{z^2}$ orbitals of Mn and $2p_y$ and $2p_x$ orbitals of O, whereas the bottom of the CB is formed mainly by empty $5d_{x^2-y^2}$ and $5d_{xy}$ orbitals of W hybridized with $3d_{x^2-y^2}$ and $3d_{xy}$ orbitals of Mn. It should be noted that the hybridization between the Mn 3d and 2p states is observed in the whole VB, further indicating that $MnWO_4$ appears to have a covalent character.

The calculated values of E_{surf}, magnetic order, spin multiplicity, number of broken bonds, bang gap energy, magnetic moment and magnetization are listed in Table 1, while the structure and undercoordinated clusters on the top of each surface are displayed in **Fig. S4**. The following stability order is then established for the $MnWO_4$ surfaces: (0 1 0) > (1 1 0) > (0 0 1) > (0 1 1) > (1 1 1) > (0 1 2) > (1 0 1) > (1 0 0).

According to our results, the (1 1 0), (0 0 1), (0 1 1), (0 1 2) and (1 0 0) surfaces have AFM singlet states ($2S + 1 = 1$), whereas the (0 1 0) surface is characterized by AFM sextet state ($2S + 1 = 6$). This is expected since the lowest energy state of the (0 1 0) surface containing 7 Mn atoms has uncompensated spins along the AFM surface. Regarding the (1 1 1) and (1 0 1) surfaces, they are considered high-spin FM states with spin multiplicities of 61 and 56, respectively. The total number of unpaired electrons is listed in **Table S1**.

Undercoordinated clusters generated during the cutting process of the slab model construction have strong influence on the local environment around magnetic atoms, as well as on the charge density distribution along the plane [19]. The studied surfaces present Mn atoms with three types of undercoordinated clusters: [MnO_5], [MnO_4], and [MnO_3], while W atoms could exhibit undercoordinated [WO_5] and [WO_4] clusters. We can observe that the most stable surface (the (0 1 0) plane) presents distorted [MnO_6] octahedral clusters and undercoordinated [WO_4] clusters, in addition to a lower number of broken bonds. The (1 1 0) and (1 0 1) surfaces exhibit similar undercoordinated clusters and the same number of broken bonds. However, the (1 0 1) surface has a higher E_{surf}, a feature which is certainly attributed to its FM character with different environment chemical at the magnetic atoms.

Table 1

Calculated values of E_{surf} (Jm^{-2}), band gap energy surface, E_{gap}^{surf} (eV), number of broken bonds (N_b), area (nm^2), magnetic moment per site (μ_B) and magnetization density, D_μ ($\mu_B nm^{-2}$).

Surface	E_{surf}	N_b	$2S+1$	E_{gap}^{surf}	Mn site	μ	$D_{¼}$
(0 1 0)	0.45	4	AFM/6	3.52	Mn_{6c}	−4.734	20.17
(1 1 0)	0.58	5	AFM/1	3.60	Mn_{6c}	−4.716	0.097
					Mn_{4c}	4.680	
(0 0 1)	0.85	5	AFM/1	3.59	Mn_{5c}	4.722	0.090
					Mn_{5c}	−4.697	
(0 1 1)	0.93	4	AFM/1	3.75	Mn_{6c}	4.703	0.082
					Mn_{4c}	−4.673	
(1 1 1)	1.30	5	FM/61	1.95	Mn_{5c}	4.724	21.39
					Mn_{4c}	4.013	
					$W2_{5c}$	1.035	
					$W1_{5c}$	0.117	
(0 1 2)	1.36	6	AFM/1	2.32	Mn_{6c}	4.714	4.645
					Mn_{6c}	−4.707	
					Mn_{4c}	3.672	
					W_{4c}	−0.974	
					O5	0.099	
(1 0 1)	1.54	5	FM/56	1.93	Mn_{6c}	4.712	26.00
					Mn_{4c}	3.981	
					W_{4c}	1.034	
					O9	0.127	
					O3	0.053	
					O5	−0.036	
(1 0 0)	3.46	10	AFM/1	0.26	Mn_{3c}	4.471	0.001
					Mn_{3c}	−4.470	

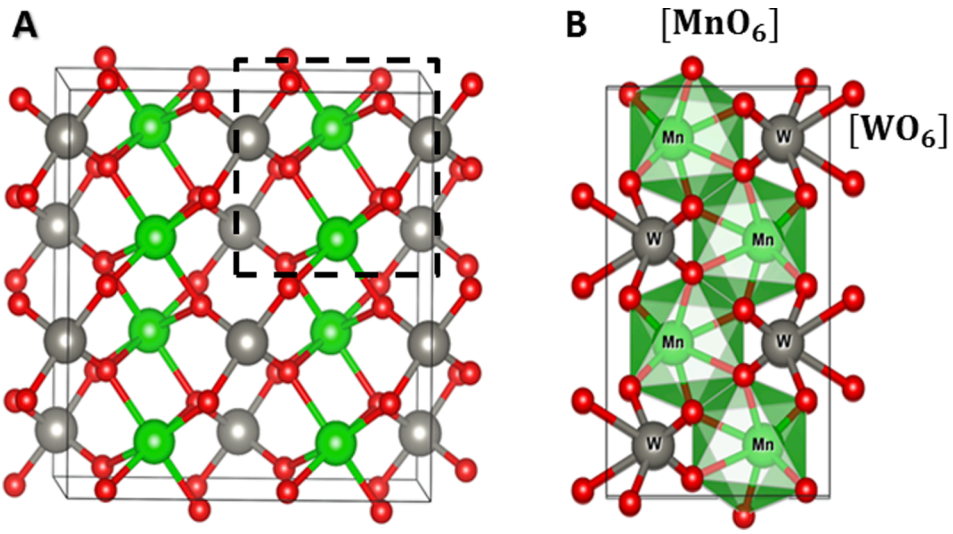

Fig. 4. (**A**) Schematic representation of the $MnWO_4$ structure using a 2x1x2 supercell model. (**B**) Zigzag chains of [MnO_6] octahedral clusters along the *a* axis. Mn atoms are in green, W atoms are in grey and O atoms are in red. The box in dotted lines represents a unit cell of $MnWO_4$ (P/2c) containing two Mn^{2+} magnetic ions. (For interpretation of the references to colour in this figure legend, the reader is referred to the web version of this article.)

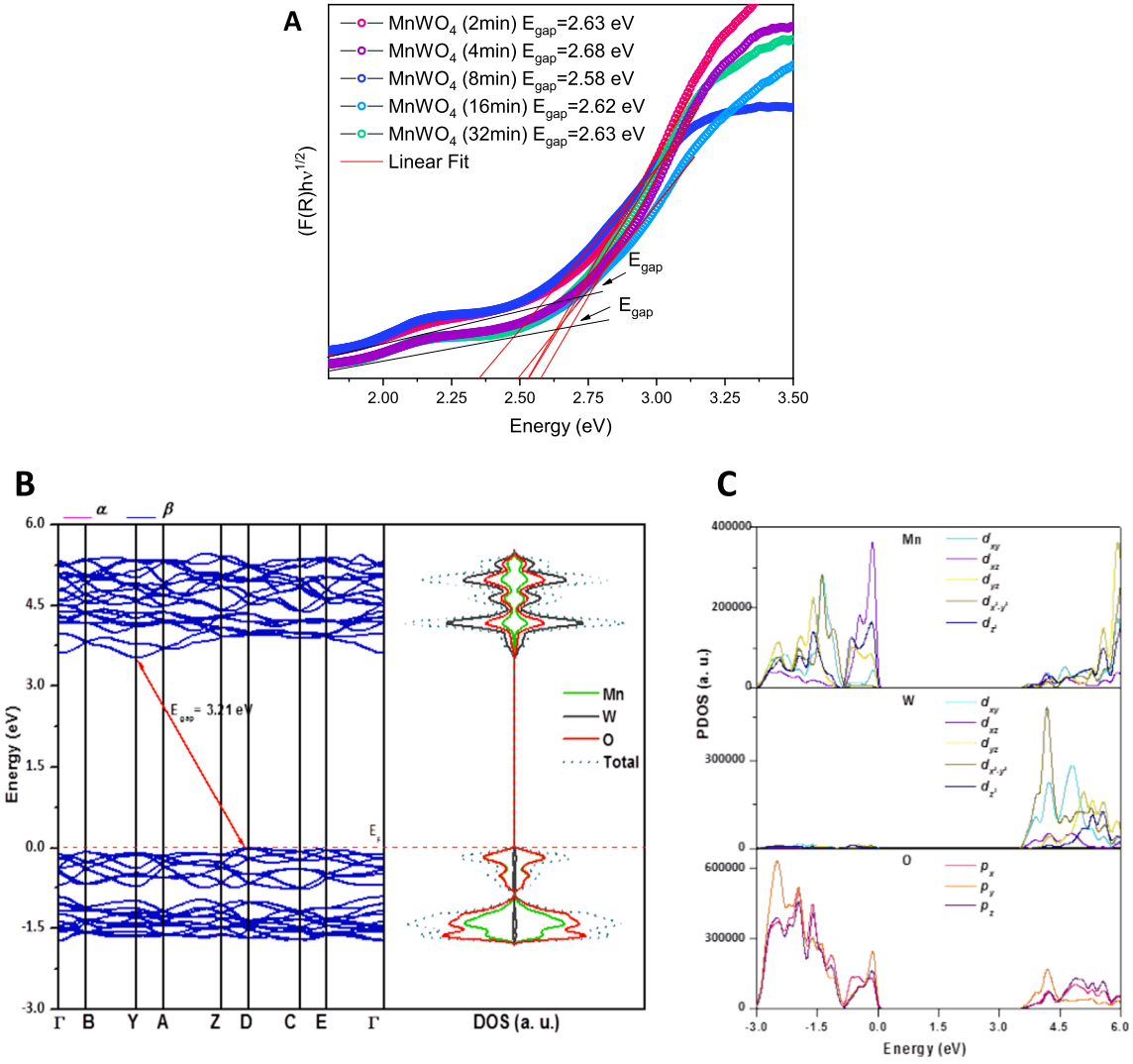

Fig. 5. (A) Energy gap estimated by the Kubelka-Munk and Wood-Tauc functions. (B) Band structure diagram (left panel) and total density of states (right panel) for $MnWO_4$. (C) Partial density of states for valence orbitals for the Mn, W, and O atoms.

On the other hand, despite having the same number of broken bonds as the (0 1 0) surface, the (0 1 1) surface shows higher E_{surf} value, which can be attributed to the greater number of exposed undercoordinated clusters and larger structural disorder at the surface. For the (0 0 1), (1 1 1) and (0 1 2) surfaces, the stability order can be established as a result of the number of broken bonds generated from undercoordinated clusters present at each surface. The (1 0 0) surface is a non-symmetrical plane composed of undercoordinated [MnO_3] clusters in the upper part of the slab, whereas the lower part is comprised of undercoordinated [WO_4] clusters. As reported in Table 1, the (1 0 0) surface has a polar character with the highest number of broken bonds, being considered the most unstable surface.

We can then conclude that the stability of the surfaces is mainly determined by the spatial disposition of the undercoordinated and distorted clusters exposed at each surface and the corresponding interatomic interactions, and that such stability does not exhibit a linear trend with respect to the number of broken bonds.

To analyze the effect of undercoordinated clusters on the electronic properties of surfaces, **Fig. S5** shows the band structure profile and calculated DOS of the different surfaces. An analysis of the results indicates that the (0 1 0), (1 1 0), (0 0 1), and (0 1 1) planes might have semiconducting behavior with E_{gap}^{surf}, a feature very similar to that predicted in bulk $MnWO_4$ (3.21 eV). We also found that the (0 1 2) surface has a reduced E_{gap}^{surf} (2.32 eV) compared to the bulk and that the (1 1 1) and (1 0 1) surfaces display the lowest value of E_{gap}^{surf} (~1.94 eV), whereas the (1 0 0) surface has a metallic character. The decrease in the band gap energy is related to the structural and electronic disorder caused by V_O, which in turn is associated with different undercoordinated clusters on the surfaces [45] responsible for altering the distribution level at the VB or CB, with concomitant appearance of intermediary levels in the band gap region (**Fig. S5E-G**). The metallic behavior observed in the (1 0 0) surface can be attributed to the increase in the Mn–O bond length, a feature that is accompanied by a decrease in the bonding-nonbonding effect of σ-and π-bonded Mn-*d* and O-*p* orbitals.

Usually, electrons in solids may participate either in bonding or magnetism [69]. Regarding the surface magnetic moment, as found and listed in Table 2, the Mn atoms in [MnO_5] clusters have magnetic moment very similar to their bulk value of 4.73 μ_B, ranging from 4.68 to 4.72 μ_B, while Mn atoms in [MnO_4] clusters have lower magnetic moments from 3.67 to 4.68 μ_B. The Mn atoms in [MnO_3] clusters, on the other hand, have a magnetic moment of 4.47μ_B. These discrepancies in the magnitude of the magnetic moments of Mn are related to the number of broken bonds in each cluster and to the structure and metal–metal interaction, which in turn establish the magnetic properties of the system through a charge density rearrangement associated with the anionic displacement and shrinkage of the bond. The bond length data of [MO_x] clusters are displayed in **Fig. S6**.

Otherwise, the [MnO_4] clusters at the (0 1 2) surface were found to have the lowest magnetic moment of Mn (3.672 μB), with its remainder magnetic moment localized at O and largely at W atoms, as shown in **Fig. S6**. The average bond length between Mn–O (1.905 Å) in the [MnO_4] clusters is smaller than that between Mn–O (2.22 Å) in the [MnO_6] clusters. As a consequence of the bond length in the Mn–O bonding distance, an induced magnetic moment occurs in the oxygen atom of the [MnO_4] clusters. In addition, the (0 1 2) surface exhibits [WO_4] clusters, which also present a shortcoming in the W–O bond length (**Fig. S6**) and an induced magnetic moment of the W atom from the [WO_4] cluster. Such effect emphasizes the importance of the hybridization of Mn − 3*d* with W − 5*d* orbitals. A similar behavior can be observed in the case of the (1 1 1) surface, that is, the existence of [WO_5] clusters result in a reduced magnetic moment in the Mn cations, whereas the exposed undercoordinated W centers become magnetic. Such a slight increase in the local magnetic moments of W and O can be confirmed by the overlapping of the spin density distribution on W–O and Mn–O, as shown in Fig. 6**E and 6F**.

Table 2
Contribution of each surface (C_i,%), total magnetization (M,$\mu_B nm^{-2}$), polyhedron energy (E_{poly}, Jm^{-2}) and polyhedron band gap energy value (E_{gap}^{poly}, eV) for each morphology.

Morphology	Surface	$E_{surf}^{(hkl)}$	C_i	***M***	E_{poly}	E_{gap}^{poly}
Ideal $MnWO_4$	(0 1 0)	0.45	30.0	6.07	0.60	3.57
	(1 1 0)	0.58	46.3			
	(0 0 1)	0.85	23.7			
A1	(0 1 0)	0.45	29.7	10.4	0.63	3.23
	(1 1 0)	0.58	35.3			
	(0 0 1)	0.85	14.1			
	(0 1 1)	0.93	0.18			
	(1 1 1)	0.81	20.7			
A2	(0 1 0)	0.55	6.90	21.3	0.45	2.06
	(1 1 1)	0.44	93.1			
A3	(1 1 1)	0.43	100	21.6	0.42	1.95
B1	(0 1 0)	0.80	19.6	11.5	0.94	3.24
	(1 1 0)	1.12	17.0			
	(0 0 1)	0.85	14.4			
	(0 1 1)	0.93	19.9			
	(1 0 1)	1.00	29.1			
B2	(0 1 0)	0.88	15.0	18.2	0.64	2.65
	(0 1 1)	0.93	26.6			
	(1 0 1)	0.45	58.4			
B3	(0 1 0)	0.97	15.0	23.2	0.53	2.30
	(0 1 1)	0.85	7.40			
	(1 0 1)	0.41	77.6			
C1	(0 1 0)	0.45	46.2	19.1	0.65	2.57
	(1 1 0)	0.95	4.55			
	(0 0 1)	0.84	11.5			
	(1 0 1)	0.81	27.8			
C2	(0 1 0)	0.50	36.7	23.9	0.55	2.51
	(1 0 1)	0.58	63.3			
C3	(0 1 0)	0.92	23.6	24.7	0.66	2.43
	(1 0 1)	0.58	76.4			
D1	(0 1 0)	0.45	46.2	16.1	0.78	3.02
	(0 0 1)	0.85	4.55			
	(1 1 1)	1.30	11.5			
	(0 1 2)	0.91	27.8			
D2	(0 1 0)	0.65	27.7	13.7	0.83	2.55
	(1 1 1)	1.30	28.6			
	(0 1 2)	0.65	43.7			
D3	(1 1 1)	1.30	23.6	8.10	0.63	2.24
	(0 1 2)	0.45	76.3			
E1	(0 1 0)	0.45	51.5	10.9	0.71	2.88
	(0 0 1)	0.83	27.1			
	(1 1 1)	1.30	2.30			
	(1 0 0)	1.15	19.1			
E2	(0 1 0)	0.45	43.5	13.6	0.72	2.53
	(1 1 1)	1.06	16.5			
	(0 1 2)	0.76	27.7			
	(1 0 0)	1.15	12.2			

Nonetheless, we must emphasize that even though both (011) and (101) surfaces exhibit the same kind of the undercoordinated clusters ([MnO_4], [WO_4], and [WO_5]), the magnetic moments in the two Mn clusters are different mainly because of two features: (i) the Mn atoms are not equivalent in both clusters; and (ii) the distribution of neighboring atoms is not same. This implies that they have different interactions with W and O atoms; therefore, the total magnetic moments of Mn atoms at surfaces are mainly a result between the local magnetic moments of Mn and the overlapping between the orbitals of Mn, O, and W atoms located along the surface.

To further explore the magnetic properties of $MnWO_4$, the spin charge density distribution of the surfaces is displayed in Fig. 6. The results indicate that the interactions between Mn atoms and their neighboring W atoms play a crucial role in their magnetic properties. For the surface along (1 0 1), the superexchange interaction is established between the paramagnetic oxygen (O3) ion, which in turn is linked to two magnetic Mn1 and Mn3 ions (Mn1 – O3 –Mn3). Therefore, each *d*-electron interacts with one of the two *p*-electrons of the spin-saturated outermost electron pair of the oxygen O3 according to the Pauli

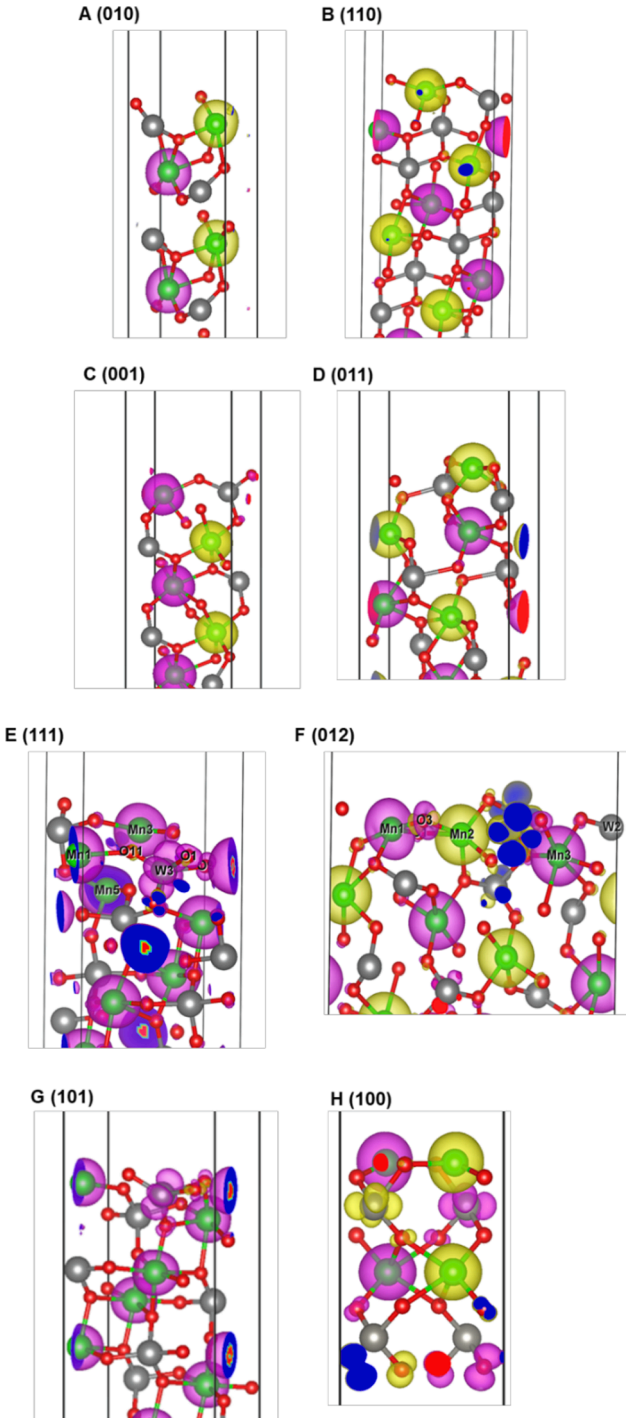

Fig. 6. Spin density for (A) (0 1 0), (B) (1 1 0), (C) (0 0 1), (D) (1 1 1), (E) (0 1 1), (F) (0 1 2), (G) (1 0 1), and (H) (1 0 0) surfaces of $MnWO_4$. Mn atoms are in green, W atoms are in grey, and O atoms are in red. Alpha spin density is in pink, while beta spin density in yellow. (For interpretation of the references to colour in this figure legend, the reader is referred to the web version of this article.)

principle [70]. This can be classified as a strong interaction, meaning that the magnetic moment of Mn atoms decreases and becomes smaller than that of the paramagnetic substance.

It is important to notice that *d–d* interactions between Mn-3*d* and W-5*d* orbitals occur along (1 1 1), (0 1 2), and (1 0 1) surfaces, leading to delocalized impurity bands in the band structure and DOS, as shown in **Fig. S4.** Moreover, a $^6A_1 \rightarrow {}^4T_1$ transition associated with the 3*d* states of Mn^{2+} is expected to take place since the states within the 3*d* shell are strongly affected by the local crystal field environment associated with the Mn^{2+} ions, a feature already observed in other mixed oxides of Mn [19]. Therefore, the combination of the surface chemical environment and its singular electronic structure distributions allows to tailor the overall superficial magnetism of $MnWO_4$ nanoparticles, thus improving their practical applications.

By tuning the values of E_{surf}, the polar (1 0 0) surface and the (0 1 0), (1 1 1), (0 1 2) and (1 0 1) surfaces with non-zero value of the magnetic moment, we were able to construct a complete map of available morphologies of $MnWO_4$ (Fig. 7). The combination between the morphology and the spin densities,E_{surf} and E_{gap}^{surf} values of the exposed surfaces allowed us to calculate the total magnetization density index (M), E_{poly} and E_{gap}^{poly}, respectively, for each morphology displayed in Fig. 7. Table 2 summarizes the percentage values of contribution of each surface (C_i), E_{surf}, M, E_{poly} and E_{gap}^{poly} for each morphology.

It is known that the ideal morphology of $MnWO_4$ is hexagonal. By taking into consideration the contributions to the magnetic moment from its exposed (010), (110), and (001) surfaces, it is possible to conclude that the total magnetic moment reaches values as high as 6.09 μ_B, primarily originated from uncompensated spins along the (010) surface. Given the stabilization of the (111) surface and the control of the E_{surf} of (010), we were able to find the A3 shape, which has an octahedral shape with the exclusively exposed (111) surface and a value of $M = 21.6$ μ_B. B3 morphologies corresponding to a corner-truncated nanorod with exposed (010), (012), and (101) surfaces present a surface magnetism corresponding to 23.2 μ_B. The cubic shape of the C3 morphology with $M = 24.7$ μ_B is predominantly formed by the (1 0 1) and (010) surfaces. On the other hand, the D3 morphology is composed of the (012) and (111) surfaces and has a value of magnetic moment of $M = 8.11$ μ_B. Finally, the E1 and E2 morphological shapes predominantly exhibit the (0 1 0) surface and have magnetic moments of $M =$ 10.9 and 13.6 μ_B, respectively. It is also important to emphasize that the B2 and B3 morphologies show excellent agreement with the FE-SEM and HR-TEM experimental images for samples synthesized at 2 min and 32 min, respectively, in addition to evidencing the increase in particle size along in the (0 1 0) direction. Therefore, the deep defects created by the MI (evidenced by the PL), increase the contribution of the surface (0 1 0), and modify the value of M at the final morphology, as it is theoretically calculated and evidenced experimentally.

The analysis of the calculated magnetization index (M) listed in Table 2 for the morphologies in Fig. 7 indicates that the A3, B3, and C3 morphologies show the highest values for M, which is certainly attributed to the highest magnetic moment of the (1 0 1) surface. In contrast, the D3 morphology exhibits the lowest value of M. These results suggest that the precise control of the superficial structure and morphology of $MnWO_4$ specimens with reduced lengths play an important role in the design of the overall properties of the material.

From the calculated values of E_{poly} in Table 2 we were able to obtain the energy profiles that link the ideal morphology of $MnWO_4$ to the different morphologies shown in Fig. 7. These energy profiles can provide information on the morphology transformation from thermodynamic and kinetic points of view [37], required for the controlled synthesis of materials with improved properties. Fig. 8 illustrates the reaction paths obtained.

In reaction path A, two morphologies (A2 and A3) with lower E_{poly} than the ideal $MnWO_4$ morphology were obtained by stabilizing the (1 1 1) surface and increasing the E_{surf} of the (0 1 0) surface. To achieve the experimental FE-SEM morphology (reaction path B), it was first necessary to increase the E_{surf} of the (0 1 0) and (1 1 0) surfaces and decrease the value associated with the (1 0 1) surface (B1). Changes in E_{surf} values were found to increase the magnitude of the E_{poly}, resulting in a maximum point. The next stage involved the increase in the E_{surf} of the (0 1 0) surface and the decrease in the E_{surf} of the (1 0 1) surface (B2). In

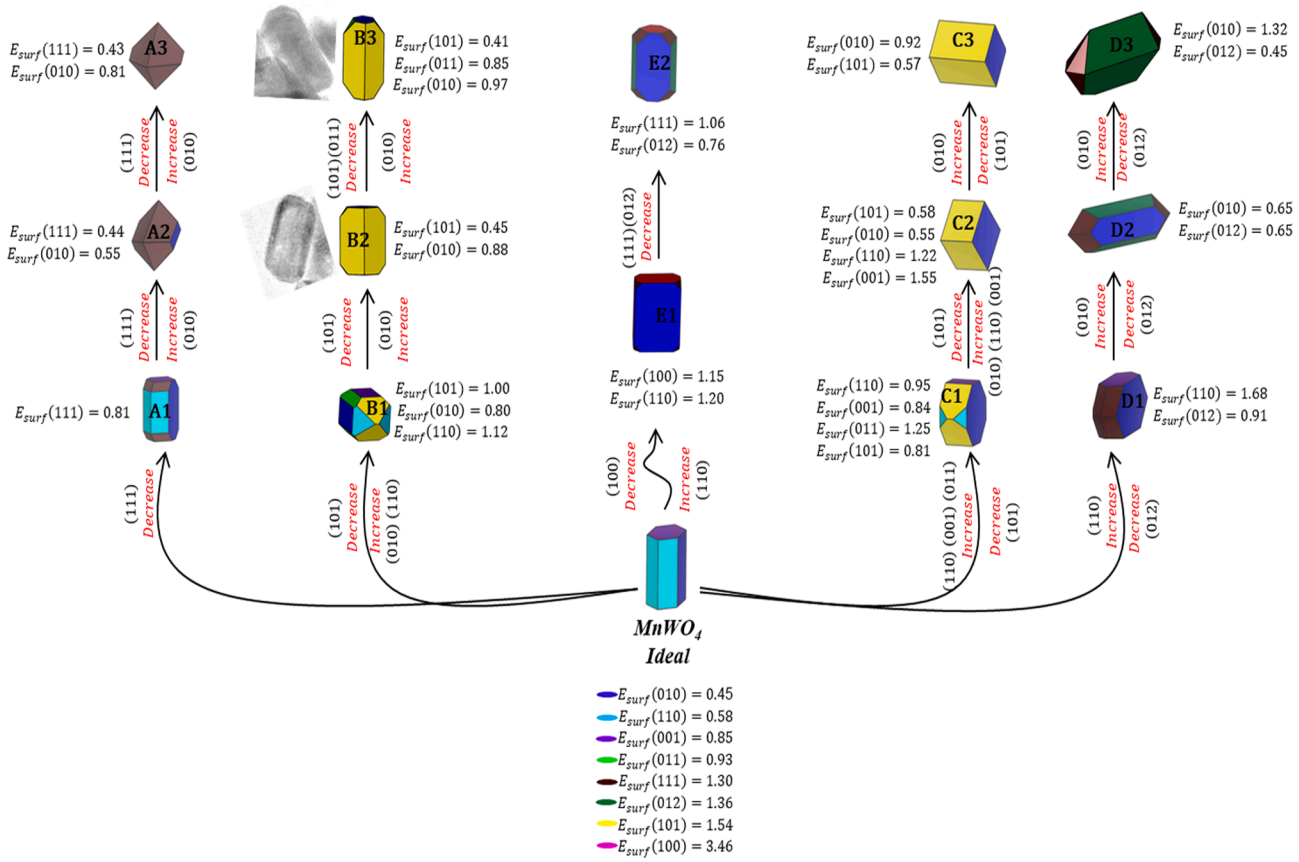

Fig. 7. Complete map of available morphologies of $MnWO_4$ obtained by tuning the E_{surf} values of (0 1 0), (1 1 0), (0 0 1), (0 1 1), (1 1 1), (0 1 2), (1 0 1) and (1 0 0) surfaces. The surface energy (E_{surf}) is in Jm^{-2}.

the last stage, there was a decrease in the E_{surf} of the (1 0 1) and (0 1 1) surfaces, leading to the obtention of the experimental morphology (B3). The B2 and B3 morphologies predominantly exposed the (1 0 1) surface, with a minor proportion of the (0 1 0) and (0 1 1) surfaces. Whereas the B2 morphology showed an E_{poly} similar to the ideal $MnWO_4$ morphology, the B3 exhibited a lower E_{poly}, denoting a higher stability.

In the case of reaction path C, two morphologies mainly exposing the (1 0 1) and (0 1 0) surfaces were obtained (C2 and C3). The C2 morphology, which exposed the (1 0 1) surface in lower proportion than the C3 morphology, showed a lower E_{poly} than the ideal $MnWO_4$ morphology. Reaction path D passed along one maximum (D2), involving an E_{surf} increase in the (1 1 0) and (0 1 0) surfaces and an E_{surf} decrease in the (0 1 2) surface. Subsequently, the (0 1 2) surface was stabilized to obtain the final morphology (D3), which exhibited a higher proportion of the (0 1 2) surface and showed a stability similar to the ideal $MnWO_4$ morphology. Finally, in reaction path E morphologies with higher E_{poly} were obtained by stabilizing the polar (1 0 0) surface (E1), followed by an E_{surf} decrease in the (1 1 1) and (0 1 2) surfaces (E2).

It is worth mentioning that the morphology of the studied specimens may have been responsible for changes in the energy band gap of materials. The calculated values of energy band gap for different theoretical morphologies of $MnWO_4$ are listed in Table 2. Computational calculations indicate that E_{gap}^{poly} value for ideal morphology of $MnWO_4$ is 3.57 eV, which is in good agreement with the calculated E_{gap} value for bulk $MnWO_4$ (3.21 eV). In particular, the A3 morphology with $E_{gap}^{poly} = 1.95$ eV exhibited the lowest band gap value, as it exclusively exposed the (1 1 1) surface. The B2 and B3 morphologies exhibited E_{gap}^{poly} values of 2.65 and 2.30 eV, respectively, which are consistent with our experimental results. The values of band gap size are important, provided that they determine the light absorption range of semiconductors and the number of photo-generated electron/hole pairs, which are the main factors responsible for the photocatalytic activity of the materials. These results demonstrate that a precise control of the surface structure and morphology of $MnWO_4$ is essential to enhance the overall properties of the material.

4. Conclusions

Herein, a combined experimental and computational approach for the analysis of $MnWO_4$ model-type metal oxide systems synthesized via a co-precipitation method was reported in order to highlight the most relevant factors to tune and link the optical, electronic and magnetic properties of this semiconducting material. First principle DFT calculations were carried out on appropriate bulk and surface models of $MnWO_4$. The (0 0 1), (0 1 0), (1 0 0), (0 1 1), (1 0 1), (1 1 0), (0 1 2) and (1 1 1) surfaces of $MnWO_4$ were selected for the modulation of these properties. The relative stability of these surfaces was calculated to develop a complete map of available morphologies and rationalize the crystal morphologies observed in FE-SEM images using the Wulff construction. Theoretical calculations suggested that the electronic and magnetic properties of the materials analyzed strongly depend on the geometry of exposed surfaces at the morphology. This correlation was found to be related to the surface energy and the type of clusters, i.e., local coordination of unsaturated superficial Mn and W cations. Finally, as our model system is not limited to the development of $MnWO_4$-based materials, the new highly effective method presented herein might help to identify suitable materials with improved electrical and magnetic properties.

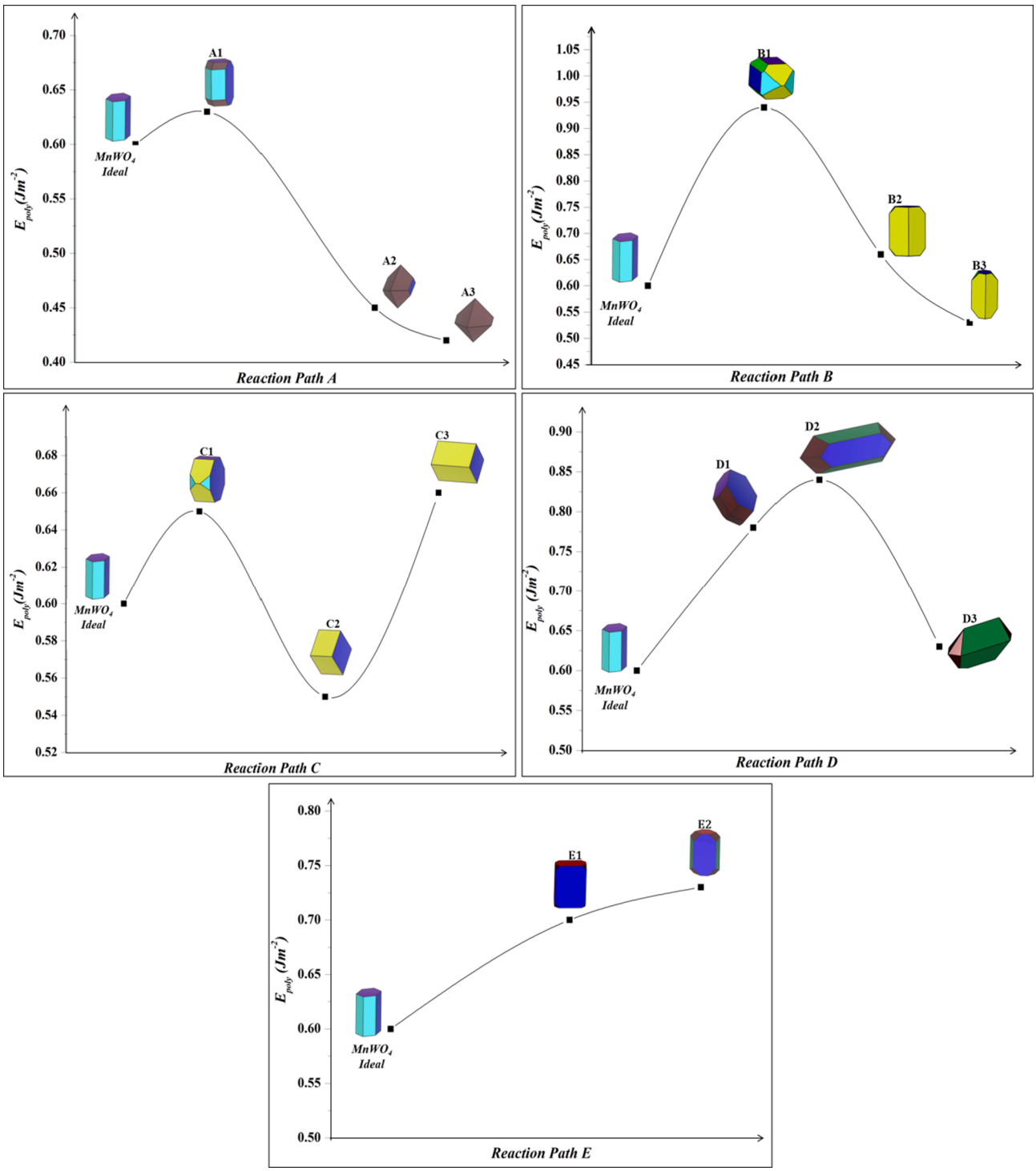

Fig. 8. . Schematic representation of the energy profile to obtain different morphologies for $MnWO_4$.

CRediT authorship contribution statement

Marcelo Assis: Investigation, Project administration, Methodology, Validation, Data curation, Visualization, Writing – original draft, Writing – review & editing. **Ana C.M. Tello:** Methodology, Validation, Formal analysis, Investigation, Writing – original draft, Writing – review & editing. **Fabio S.A. Abud:** Methodology, Validation, Formal analysis, Investigation, Writing – original draft, Writing – review & editing. **Pablo Negre:** Methodology, Validation, Formal analysis. **Lara K. Ribeiro:** Methodology, Validation, Formal analysis. **Renan A.P. Ribeiro:** Methodology, Validation, Formal analysis, Investigation, Writing – original draft, Writing – review & editing. **Sueli H. Masunaga:** Methodology, Validation, Formal analysis, Investigation, Writing – original draft, Writing – review & editing. **Aline E.B. Lima:** Methodology, Validation, Formal analysis. **Geraldo E. Luz Jr:** Methodology, Validation, Formal analysis. **Renato F. Jardim:** Methodology, Validation, Data curation, Visualization, Funding acquisition, Writing – original draft, Writing – review & editing. **Albérico B.F. Silva:** Validation, Formal analysis. **Juan Andrés:** Methodology, Validation, Data curation, Visualization, Funding acquisition, Writing – original draft, Writing –

review & editing. **Elson Longo:** Methodology, Validation, Data curation, Visualization, Funding acquisition, Writing – original draft, Writing – review & editing.

Declaration of Competing Interest

The authors declare that they have no known competing financial interests or personal relationships that could have appeared to influence the work reported in this paper.

Acknowledgment

This work was funded in part by Fundação de Amparo à Pesquisa do Estado de São Paulo - FAPESP (2013/07296-2), Financiadora de Estudos e Projetos - FINEP, Conselho Nacional de Desenvolvimento Cientifico e Tecnológico - CNPq, and Coordenação de Aperfeiçoamento de Pessoal de Nível Superior - CAPES (finance code 001). J.A. acknowledges Universitat Jaume I (project UJI-B2019-30), and the Ministerio de Ciencia, Innovación y Universidades (Spain) (project PGC2018094417-B-I00) for financially supporting this research. M.A. was supported by the Margarita Salas postdoctoral contract MGS/2021/21 (UP2021-021) financed by the European Union-NextGenerationEU. R. A. P. R. acknowledges FAPEMIG (APQ-00079-21) and UEMG (Productivity Program) for the financial assistance.

Appendix A. Supplementary material

Supplementary data to this article can be found online at https://doi.org/10.1016/j.apsusc.2022.154081.

References

[1] S. Muthamizh, R. Suresh, K. Giribabu, R. Manigandan, S. Praveen Kumar, S. Munusamy, V. Narayanan, $MnWO_4$ nanocapsules: synthesis, characterization and its electrochemical sensing property, J. Alloys Compd. 619 (2015) 601–609.
[2] K.K. Naik, A.S. Gangan, A. Pathak, B. Chakraborty, S.K. Nayak, C.S. Rout, Facile hydrothermal synthesis of $MnWO_4$ nanorods for non-enzymatic glucose sensing and supercapacitor properties with insights from density functional theory simulations, ChemistrySelect 2 (2017) 5707–5715.
[3] M.A.P. Almeida, L.S. Cavalcante, J.A. Varela, M.S. Li, E. Longo, Effect of different surfactants on the shape, growth and photoluminescence behavior of MnWO4 crystals synthesized by the microwave-hydrothermal method, Adv. Powder Technol. 23 (2012) 124–128.
[4] J. Yesuraj, E. Elanthamilan, B. Muthuraaman, S.A. Suthanthiraraj, J.P. Merlin, Bio-assisted hydrothermal synthesis and characterization of $MnWO_4$ nanorods for high-performance supercapacitor applications, J. Electron. Mater. 48 (2019) 7239–7249.
[5] P. Patureau, R. Dessapt, P. Deniard, U.C. Chung, D. Michau, M. Josse, C. Payen, M. Maglione, Persistent Type-II multiferroicity in nanostructured $MnWO_4$ ceramics, Chem. Mater. 28 (2016) 7582–7585.
[6] J. Ungelenk, S. Roming, P. Adler, W. Schnelle, J. Winterlik, C. Felser, C. Feldmann, Ultrafine $MnWO_4$ nanoparticles and their magnetic properties, Solid State Sci. 46 (2015) 89–94.
[7] O. Heyer, N. Hollmann, I. Klassen, S. Jodlauk, L. Bohaty, P. Becker, J. Mydosh, T. Lorenz, D. Khomskii, A new multiferroic material: $MnWO_4$, J. Phys. Condens. Matter. 18 (2006) L471–L475.
[8] G. Lautenschläger, H. Weitzel, T. Vogt, R. Hock, A. Böhm, M. Bonnet, H. Fuess, Magnetic phase transitions of $MnWO_4$ studied by the use of neutron diffraction, Phys. Rev. B. 48 (1993) 6087–6098.
[9] S. Lei, K. Tang, Z. Fang, Y. Huang, H. Zheng, Synthesis of $MnWO_4$ nanofibres by a surfactant-assisted complexation-precipitation approach and control of morphology, Nanotechnology 16 (2005) 2407–2411.
[10] D. Meziani, Y. Roumila, N.Y. Ghoul, D. Benmeriem, K. Abdmeziem, M. Trari, Physicochemical characterizations and semiconducting properties of a manganese tungstate $MnWO_4$ obtained by hydrothermal route, J. Solid State Electrochem. 25 (2021) 2097–2106.
[11] J. Ungelenk, M. Speldrich, R. Dronskowski, C. Feldmann, Polyol-mediated low-temperature synthesis of crystalline tungstate nanoparticles $MnWO_4$ (M = Mn, Fe Co, Ni, Cu, Zn), Solid State Sci. 31 (2014) 62–69.
[12] S. Thongtem, S. Wannapop, A. Phuruangrat, T. Thongtem, Cyclic microwave-assisted spray synthesis of nanostructured $MnWO_4$, Mater. Lett. 63 (2009) 833–836.
[13] P. Parhi, T.N. Karthik, V. Manivannan, Synthesis and characterization of metal tungstates by novel solid-state metathetic approach, J. Alloys Compd. 465 (2008) 380–386.
[14] W. Qu, W. Wlodarski, J.-U. Meyer, Comparative study on micromorphology and humidity sensitive properties of thin-film and thick-film humidity sensors based on semiconducting $MnWO_4$, Sens. Actuators B Chem. 64 (2000) 76–82.
[15] S. Poovaragan, R. Sundaram, Optical, magnetic and humidity sensing properties of $MnWO_4$–WO_3 composites, Adv. Sci. Eng. Med. 11 (2019) 255–260.
[16] W.B. Hu, X.L. Nie, Y.Z. Mi, Controlled Synthesis and structure characterization of nanostructured $MnWO_4$, Mater. Charact. 61 (2010) 85–89.
[17] J. Mao, J. Zhao, L. Li, T. Chen, Q. Lv, Y. Li, Effect of Different surfactants on the morphology, growth and magnetic behavior of MnWO $MnWO_4$ crystals via the hydrothermal method, Chin. J. Phys. 63 (2020) 163–167.
[18] H. Zhou, Y. Yiu, M.C. Aronson, S.S. Wong, Ambient template synthesis of multiferroic $MnWO_4$ nanowires and nanowire arrays, J. Solid State Chem. 181 (2008) 1539–1545.
[19] R.A.P. Ribeiro, J. Andrés, E. Longo, S.R. Lazaro, Magnetism and Multiferroic Properties at $MnTiO_3$ surfaces: A DFT study, Appl. Surf. Sci. 452 (2018) 463–472.
[20] V.S.C. Kolluru, R. Henning, Role of magnetism on transition metal oxide surfaces in vacuum and solvent, Phys. Rev. Mater. 4 (2020), 045803.
[21] R.A.P. Ribeito, R. Hennig, Towards enhancing the magnetic properties by morphology control of $ATiO_3$ (A=Mn, Fe, Ni) multiferroic materials, J. Magn. Magn. Mater. 475 (2019,) 544–549.
[22] A. Soon, X.-Y. Cui, B. Delley, S.-H. Wei, C. Stampfl, Native defect induced multifarious magnetism in nonstoichiometric cuprous oxide: first principles study of bulk and surface properties of $Cu_{2-\delta}O$, Phys. Rev. B. 79 (2009), 035205.
[23] F. Zasada, J. Gryboś, P. Indyka, W. Piskorz, J. Kaczmarczyk, Z. Sojka, Surface structure and morphology of M[CoM']O_4 (M=Mg, Zn, Fe, Co and M'= Ni, Al, Mn, Co) Spinerl nanocrystals DFT+U and TEM screening investigations, J. Phys. Chem. C. 118 (2014) 19085–19097.
[24] Z. Wang, K. Lv, G. Wang, K. Deng, D. Tang, Study on the shape control and photocaralytic activity of high-energy anatase titania, Appl. Catal. 100 (2010) 378–385.
[25] A.A.G. Santiago, R.L. Tranquilin, M.C. Oliveira, R.A.P. Ribeiro, S.R. de Lazaro, M. A. Correa, F. Bohn, E. Longo, F.V. Motta, M.R.D. Bomio, Discloding the structural, electronic and morphological properties of $CuMnO_2$: a unified experimental and theoretical approach, J. Phys. Chem. C. 124 (2020) 5378–5388.
[26] K. Manjunatha, V.J. Angadi, M. Oliveira, S. de Lazaro, E. Longo, R. Ribeiro, N. Ayachit, Towards shape-oriented Bi-Doped-$CoCr_2O_4$ nanoparticles from theoretical and experimental perspectives: structural morphological, optical, electrical and magnetic properties, J. Mater. Chem. C. 9 (2021) 6452.
[27] J. Ruiz-Fuertes, S. López, J. Lopez-Solano, D. Errandonea, A. Segura, R. Lacomba-Perales, A. Munoz, S. Radescu, P. Rodriguez, M. Gospodinov, L. Nagornaya, C. Tu, Pressure effects on the electronic and optical properties of AWO_4 Wolframites (A= Cd, Mg, Mn, and Zn): the distinctive behavior of multiferroic $MnWO_4$, Phys. Rev. B 86 (2012), 125202.
[28] L. Cai, X. Tang, C. Liu, R. Lin, Hydrostatic-pressure-dependent electronic and optical properties of tungstate $MnWO_4$: a first-principles study, Chin. J. Phys. 57 (2019) 157–164.
[29] X.Y. Qiu, H.W. Huang, Y.D. Gao, Effects of surface properties of (010), (001) and (100) of $MnWO_4$ and $FeWO_4$ on absorption of collector, Appl. Surf. Sci. 367 (2016) 354–361.
[30] T. Xin, H.E. Fa-Yu, X.I. Yu, Structural and Electronic Properties of $MnWO_4$ (010) Surface Studied by First-Principles Calculation, Metal Mine 44 (2015) 52–58.
[31] C. Lee, W. Yang, R.G. Parr, Development of the Colle-Salvetti Correlation-Energy Formula into a Functional of the Electron Density, Phys. Rev. B 37 (1988) 785–789.
[32] R. Dovesi, A. Erba, R. Orlando, C.M. Zicovich-Wilson, B. Civalleri, L. Maschio, M. Rérat, S. Casassa, J. Baima, S. Salustro, B. Kirtman, Quantum-Mechanical Condensed Matter Simulations with CRYSTAL, WIREs. Comput. Mol. Sci. 8 (2018), e1360.
[33] R.I. Eglitis, A.I. Popov, Systematic Trends in (001) Surface Ab Initio Calculations of ABO3 Perovskites, J. Saudi Chem. Society. 22 (2018) 459–468.
[34] R. Eglitis, Ab Initio Calculations of the Atomic and Electronic Structure of $BaZrO_3$ (111) Surfaces, Solid State Ion. 230 (2013) 43.
[35] L.H.S. Lacerda, M.A. San-Miguel, Approaches Unrelaveling the Surface and Morphological Properties of $MnMnO_4$, Appl. Surf. Sci. 567 (2021), 150882.
[36] E. Heifets, E.A. Kotomin, A.A. Bagaturyants, J. Maier, Ab Initio Study of BiFeO3: Thermodinamic Stability Condictions, J. Phys. Chem. Lett. 6 (2015) 2847–2851.
[37] R.A.P. Ribeiro, M.C. Oliveira, M.R.D. Bomio, S.R. de Lazaro, J. Andrés, E. Longo, Connecting the surface structure, morphology and photocatalytic activity of Ag_2O: an in depth and unified theoretical investigation, App. Surf. Sci. 509 (2020), 145321.
[38] M.D. Towler, N.L. Allan, N.M. Harrison, V.R. Saunders, W.C. Mackrodt, E. Aprà, Ab initio Study of MnO and NiO, Phys. Rev. B. 50 (1994) 5041–5054.
[39] F. Corà, A. Patel, N.M. Harrison, R. Dovesi, C.R.A. Catlow, An ab Initio Hartree−Fock Study of the Cubic and Tetragonal Phases of Bulk Tungsten Trioxide, J. Am. Chem. Soc. 118 (1996) 12174–12182.
[40] H.J. Monkhorst, J.D. Pack, Special points for brillouin-zone integrations, Phys. Rev. B. 13 (1976) 5188–5192.
[41] A.C. Catto, M.M. Ferrer, O.F. Lopes, V.R. Mastelaro, J. Andrés, L.F. da Silva, E. Longo, W. Avansi, The role of counter-ions in crystal morphology, surface structure and photocatalytic activity of ZnO crystals grown onto a substrate, Appl. Surf. Sci. 529 (2020), 147057.
[42] F. Lipsky, L.H. da Silveira Lacerda, S.R. de Lazaro, E. Longo, J. Andrés, M.A. San-Miguel, Unraveling the relationship between exposed surfaces and the photocatalytic activity of Ag_3PO_4: an in-depth theoretical investigation, RSC Adv. 10 (2020) 30640–30649.
[43] L.O. Laier, M. Assis, C.C. Foggi, A.F. Gouveia, C.E. Vergani, L.C. Santana, L. S. Cavalcante, J. Andrés, E. Longo, Surface-dependent Properties of α-Ag2WO4: a

Joint Experimental and Theoretical Investigation, Theor. Chem. Acc. 139 (2020) 108.
[44] J. Andrés, L. Gracia, A.F. Gouveia, M.M. Ferrer, E. Longo, Effects of surface stability on the morphological transformation of metals and metal oxides as investigated by first-principles calculations, Nanotechnology 26 (40) (2015) 405703.
[45] R.A.P. Ribeiro, E. Longo, J. Andrés, S.R. de Lazaro, A DFT Investigation of the Role of Oxygen Vacancies on the Structural, Electronic and Magnetic Properties of $ATiO_3$ (A = Mn, Fe, Ni) Multiferroic Materials, Phys. Chem. Chem. Phys. 20 (2018) 28382–28392.
[46] R.A.P. Ribeiro, S.R. de Lazaro, L. Gracia, E. Longo, J. Andrés, Theoretical approach for determining the relation between the morphology and surface magnetism of Co_3O_4, J. Magn. Magn. Mater. 453 (2018) 262–267.
[47] E.O. Gomes, L. Gracia, A.D. Santiago, R.L. Tranquilin, F.V. Motta, R.A. Amoresi, E. Longo, M.R. Bomio, J. Andres, Structure, Electronic Properties, Morphology Evolution, and Photocatalytic Activity in $PbMoO_4$ and $Pb_{1-2x}Ca_xSr_xMoO_4$ (x = 0.1, 0.2, 0.3, 0.4 and 0.5) Solid Solutions, Phys. Chem. Chem. Phys. 22 (2020) 25876–25891.
[48] A.C.M. Tello, M. Assis, R. Menasce, A.F. Gouveia, V. Teodoro, N. Jacomaci, M. A. Zaghete, J. Andrés, G.E. Marques, M.D. Teodoro, A.B.F. da Silva, J. Bettini, E. Longo, Microwave-Driven Hexagonal-to-Monoclinic Transition in BiPO4: An In-Depth Experimental Investigation and First-Principles Study, Inorg. Chem. 59 (2020) 7453–7468.
[49] J. Macavei, H. Schulz, The Crystal Structure of Wolframite Type Tungstates at High Pressure, Z. Kristallogr. Cryst. Mater. 207 (1993) 193.
[50] P. Patureau, R. Dessapt, P.-E. Petit, G. Landrot, C. Payen, P. Deniard, Evidence of Wolframite-Type Structure in Ultrasmall Nanocrystals with a Targeted Composition $MnWO_4$, Inorg. Chem. 58 (2019) 7822–7827.
[51] J. Ruiz-Fuertes, D. Errandonea, O. Gomis, A. Friedrich, F.J. Manjón, Room-Temperature Vibrational Properties of Multiferroic $MnWO_4$ Under Quasi-Hydrostatic Compression Up to 39 GPa, J. Appl. Phys. 115 (2014), 043510.
[52] P. Pereira, A. Fernandes Gouveia, M. Assis, R. Oliveira, I.M. Pinatti, M. Penha, R. Gonçalves, L. Gracia, J. Andres, E. Longo, $ZnWO_4$ nanocrystals: synthesis, morphology, and photoluminescence and photocatalytic properties, Phys. Chem. Chem. Phys. 20 (2017) 1923–1937.
[53] S. Dey, R.A. Ricciardo, H.L. Cuthbert, P.M. Woodward, Metal-to-Metal Charge Transfer in AWO4 (A = Mg, Mn Co, Ni, Cu, or Zn) Compounds with the Wolframite Structure, Inorg. Chem. 53 (2014) 4394–4399.
[54] M.A.P. Almeida, L.S. Cavalcante, M. Siu Li, J.A. Varela, E. Longo, Structural Refinement and Photoluminescence Properties of $MnWO_4$ Nanorods Obtained by Microwave-Hydrothermal Synthesis, J. Inorg. Organomet. Polym. Mater. 22 (2012) 264–271.
[55] R.C. de Oliveira, M. Assis, M.M. Teixeira, M.D.P. da Silva, M.S. Li, J. Andres, L. Gracia, E. Longo, An experimental and computational study of β-$AgVO_3$: optical properties and formation of Ag nanoparticles, J. Phys. Chem. C 120 (2016) 12254–12264.
[56] V.M. Longo, E. Orhan, L.S. Cavalcante, S.L. Porto, J.W.M. Espinosa, J.A. Varela, E. Longo, Understanding the origin of photoluminescence in disordered Ca0.60Sr0.40WO4: an experimental and first-principles study, Chem. Phys. 334 (2007) 180–188.
[57] S.d. Lazaro, J. Milanez, A.T.d. Figueiredo, V.M. Longo, V.R. Mastelaro, F.S. D. Vicente, A.C. Hernandes, J.A. Varela E.Longo, Relation between photoluminescence emission and local order-disorder in the CaTiO3 lattice modifier, Appl. Phys. Lett. 90 (2007).
[58] L. Cruz, M. Teixeira, V. Teodoro, N. Jacomaci, L. Latier, M. Assis, N. Macedo, A. Mora, L. Da Silva, G. Marques, M. Zaguete, M. Daldin Teodoro, E. Longo, Multi-Dimensional Architecture of Ag/α-Ag_2WO_4 Crystals: Insights into Microstructural, Morphology, and Photoluminescent Properties, CrystEngComm 1 (2020) 1.
[59] M. Assis, R.A. Pontes Ribeiro, M.H. Carvalho, M.M. Teixeira, Y.G. Gobato, G. A. Prando, C.R. Mendonça, L. de Boni, A.J. Aparecido de Oliveira, J. Bettini, J. Andrés, E. Longo, Unconventional magnetization generated from electron beam and femtosecond irradiation on α-Ag_2WO_4: a quantum chemical investigation, ACS Omega 5 (2020) 10052–10067.
[60] A. Llenas, J. Carreras, A simple yet counterintuitive optical feedback controller for spectrally tunable lighting systems, Opt. Eng. 58 (2019), 075104.
[61] A. Tiwari, V. Singh, T.C. Nagaiah, Tuning the $MnWO_4$ morphology and its electrocatalytic activity towards oxygen reduction reaction, J. Mater. Chem. A. 6 (2018) 2681–2692.
[62] W. Tong, L. Li, W. Hu, T. Yan, X. Guan, G. Li, Kinetic control of $MnWO_4$ nanoparticles for tailored structural properties, J. Phys. Chem. C 114 (2010) 15298–15305.
[63] R.H. Kodama, A.E. Berkowitz, J.E.J. McNiff, S. Foner, Surface spin disorder in $NiFe_2O_4$ nanoparticles, Phys. Rev. Lett. 77 (1996) 394–397.
[64] M.S. Seehra, A. Punnoose, Deviations from the Curie-law Variation of Magnetic Susceptibility in Antiferromagnetic Nanoparticles, Phys. Rev. B 64 (2001), 132410.
[65] U. Gattermann, G. Benka, A. Bauer, A. Senyshyn, S.H. Park, Magnetic Properties of the In-Doped MnWO4-type Solid Solutions $Mn_{1-3x}In_{2x}\square_xWO_4$ [□=vacancy; 0≤x≤0.11], J. Magn. Magn. Mater. 398 (2016) 167–173.
[66] P.K. Misra, Chapter 13 - Magnetic Ordering, in: P.K. Misra (Ed.), Phys. Condens. Matter, Academic Press, Boston, **2012**; pp 409-449.
[67] H. Ehrenberg, H. Weitzel, H. Fuess, Magnon Dispersion and Magnetic Phase Diagram of $MnWO_4$, Phys. B: Condens. Matter 234–236 (1997) 560–563.
[68] S. Toyoda, N. Abe, T. Arima, S. Kimura, Large Magnetochromism in Multiferroic $MnWO_4$, Phys. Rev. B 91 (2015), 054417.
[69] J.B. Goodenough, Characterization of d Electrons in Solids by Structure I. Localized vs Collective Electrons, Mater. Res. Bull. 2 (1967) 37–48.
[70] L. He, L. Guo, Competition of the Antiferromagnetic Superexchange with the Ferromagnetic Double Exchange in Dicobalt Complexes, Appl. Phys. Lett. 97 (2010), 182509.